Shahrood University of Technology

Journal of Mining and Environment (JME)

Journal homepage: www.jme.shahroodut.ac.ir

Iranian Society of Mining Engineering (IRSME)

Geological Mapping and Facies Characterization of Miocene Evaporites along Central-eastern Margin of Gulf of Suez Rift by Remote Sensing Techniques

Eman M. Kamel*, Mohamed S.H. Hammed, and Osama E.A. Attia

Faculty of Science, Cairo University, Cairo, Egypt

Article Info

Received 3 September 2023

Received in Revised form 7 October 2023

Accepted 10 November 2023

Published online 10 November 2023

DOI: 10.22044/jme.2023.13560.2505

Keywords

Sulphate index

Gypsum

Facies Mapping

Abstract

In the recent years, the use of ASTER and Landsat data have become prevalent for mapping different types of rock formations. Specifically, this study utilizes ASTER (L1B) and Landsat 8 (AOL) images to map outcrops of various gypsum facies in Ras Malaab area of west-central Sinai. These gypsum facies are part of a lithostratigraphic group called Ras Malaab, estimated to have been formed during the Miocene period. A range of image processing techniques was employed to create the final facies map including quartz and sulphate indices, composite image band combinations, band ratios, principal component analyses, decorrelation stretching, and SAM mapping followed by supervised classification. By using band combinations, mineral indices, and principal component analyses, sulphate minerals were distinguished from their surroundings. Additionally, decorrelation stretches and band ratios were used to differentiate between primary, secondary, faulted gypsum, anhydrite, and carbonates. The SAM rapid mapping algorithm was also an effective tool to distinguish between the main facies in the studied area and to differentiate between primary massive and bedded gypsum. The results of this study were summarized by creating a facies map of the area using supervised classification, which, in addition to petrographic studies, greatly aided in understanding the distribution of the different gypsum facies.

1. Introduction

Evaporite minerals precipitate in and around semi-closed to closed marginal marine or continental basins with high evaporation rate exceeding the water influx rate, which produces saline residual brine saturated with dissolved minerals [1]. An evaporite mineral is laid down from the brine when the brine becomes supersaturated with this mineral salt [1]. The outcropping Miocene evaporites cover 12% of the total area of the outcropping sedimentary rocks of Egypt [2]. The Miocene evaporites of Egypt show a wide range of facies changes vertically and horizontally, with numerous unconformities cutting through and representing changes in the sedimentary environment and/or conditions of brine due to different pulses of tectonic activity [3].

Various tools were used previously to map evaporites. On field observations, evaporites may be exposed in inaccessible areas, their outcrops are highly weathered, and sampling requires the removal of thick weathered rock layers [4-5]. Aerial photographs are used to identify and map evaporite facies; however, aerial imaging requires favorable climatic conditions or the images become unclear. Moreover, lithologic details may be masked by other features, and errors may occur in images, like unequal dimensions due to coordinates rotation, and tilt of rock layer or imaging aeroplane [4, 5]. One of the most known promising evaporite mapping tools is by using remote sensing data [3]. Like ASTER images, which cover wide spectral range (14 bands) that includes visible, short-wave infrared, thermal bands, and backwards-looking near-infrared band for stereo coverage. It can be observed that the spatial resolution is directly proportional to the wavelength of a given radiation or band.

* Corresponding author: emanmostafa454@gmail.com (E. Kamel)

In the present study, ASTER (L1B) and Landsat 8 (AOL) images are used. The study aims to map the different gypsum facies in Ras Malaab area. Many authors studying evaporites face the challenge of differentiating between primary and secondary evaporites. Various methodologies were previously used by many authors for this purpose, like field observations [3], petrographic studies [7], and fluid inclusion studies [8]. In the present study, ASTER and Landsat image processing is used to map the evaporite facies in Ras Malaab area and to differentiate primary from secondary/tertiary evaporite generations. This mapping method relays on discriminating the evaporite spectral signature differences in the SWIR range, caused by deformation, dehydration or recrystallization.

2. Geologic Setting

The Middle-Late Miocene evaporite deposits have widespread outcrops on both sides of the Gulf of Suez. These sediments represent the huge thickness of syn/post-rift succession of Ras Malaab Group [9]. The area of study lies on the eastern side of the Gulf of Suez, between Latitudes: 28° 15' 20" N - 28° 22' 78" N and Longitudes: 31° 51' 20" E - 31° 58' 23" E (Figure 1a).

The Gulf of Suez rift basin was formed due to different tectonic (fault) trends, which are: Aqaba fault trend is a set of oblique (normal-sinistral) faults, parallel to the central axis of Aqaba Gulf [10], affecting Southern and Central Gulf of Suez. The clysmic fault trend is a set of major normal dip-slip faults parallel to the Gulf of Suez rift axis [11]. They are the main tectonic trend that developed the Gulf of Suez rift, rift shoulders, and elongated rift basin [12]. Duwi fault trend is a set of oblique (dextral-normal) faults [13]; it is a part of the Dead Sea Shear zone (Wrench), showing En echelon arrangement WNW-ESE [14], and cutting through the central Gulf of Suez. Cross fault trend is a set of oblique (normal - dextral/sinistral) faults perpendicular to the Gulf of Suez axis [15], and affecting only the Southern Gulf of Suez.

Owing to these different tectonic trends, Gulf of Suez is divided into three sub-basins, each is a mega half-graben, with major bounding Clysmic faults switching sides along the Gulf [16-17-18]. Two tectonic accommodation hinge zones trending SW-NE separate the mega half-grabens. The dip provinces and accommodation zones are arranged from North to South as follows: Araba dip province with Clysmic fault trend, and strata dip SW [19]. Galala-Abu Zeneima (Zaafarana) accommodation zone is a basement EW trending plateau [19, 20, 21, 22, 23]; it transfers major faults throw between half-grabens with opposite tilt [24]. October (Balayim) dip province with Clysmic, Duwi and Aqaba trends, and strata dip NE [19]. Morgan accommodation zone trending ENE [19-20-21-22-23]. Amal-Zeit dip province with Clysmic, Aqaba, and cross-fault trends and strata dip SW [19]. The area of study belongs to the northern-central Gulf of Suez (Araba-October provinces); therefore, it is affected by Clysmic, Duwi, and Aqaba fault trends (Figure 1b).

The sedimentary rocks in the studied area belong to Gharandal and Ras Malaab stratigraphic mega-sequences; however, the outcropping evaporites under study belong to Ras Malaab mega-sequence. Each of the two mega-sequences represents a pulse of of the Gulf of Suez rifting [26]. Gharandal mega-sequence was deposited in clysmic fault-bound offshore basins, while the embryonic Gulf of Suez rift began to propagate in the late Oligocene [15] until middle Miocene [27]. Ras Malaab mega-sequence was deposited clysmic fault-bound onshore basins (Figure 1.b) during rejuvenated rifting in the middle Miocene until the late Miocene [8].

Gharandal group is not outcropping, but it was observed during sub-surface studies by many authors. However, other authors recorded Gharandal group outcrops along the two sides of Gulf of Suez in further southern portions of the Gulf. Oligocene Abu Zeneima Formation of aeolian deposits [28] is the pre-Gharandal lowstand stratigraphic unit. It is overlain by Gharandal group at unconformity surface with basaltic flows, sills, and dikes [15], evidence of Gulf of Suez rifting initiation. Early Miocene Nukhul formation shows facies change from lowstand fluvial and estuarine sandstone [29] to anhydrite and limestone in fault-controlled sub-basins on marginal marine zones [8]. This shows increased rift activity and sea transgression. Early-Middle Miocene Rudeis Formation deposited during active rifting in half-grabens in nerretic-bathyal setting with vertical facies change from Globigerina marl [30] to conglomerate [8]. Angular unconformity surface caused by tectonic activity (mid-clysmic event) between lower, and upper Rudeis Members decreased the rate of rifting [31]. Middle Miocene Kareem Formation lowstand rock unit unconformably overlies Rudeis Formation due to rift shoulders uplift marked with igneous rock debris and sandstone layers. At the bottom of Kareem Formation, sabkha anhydrite, and calcareous greenish shale [32] reflect sea regression.

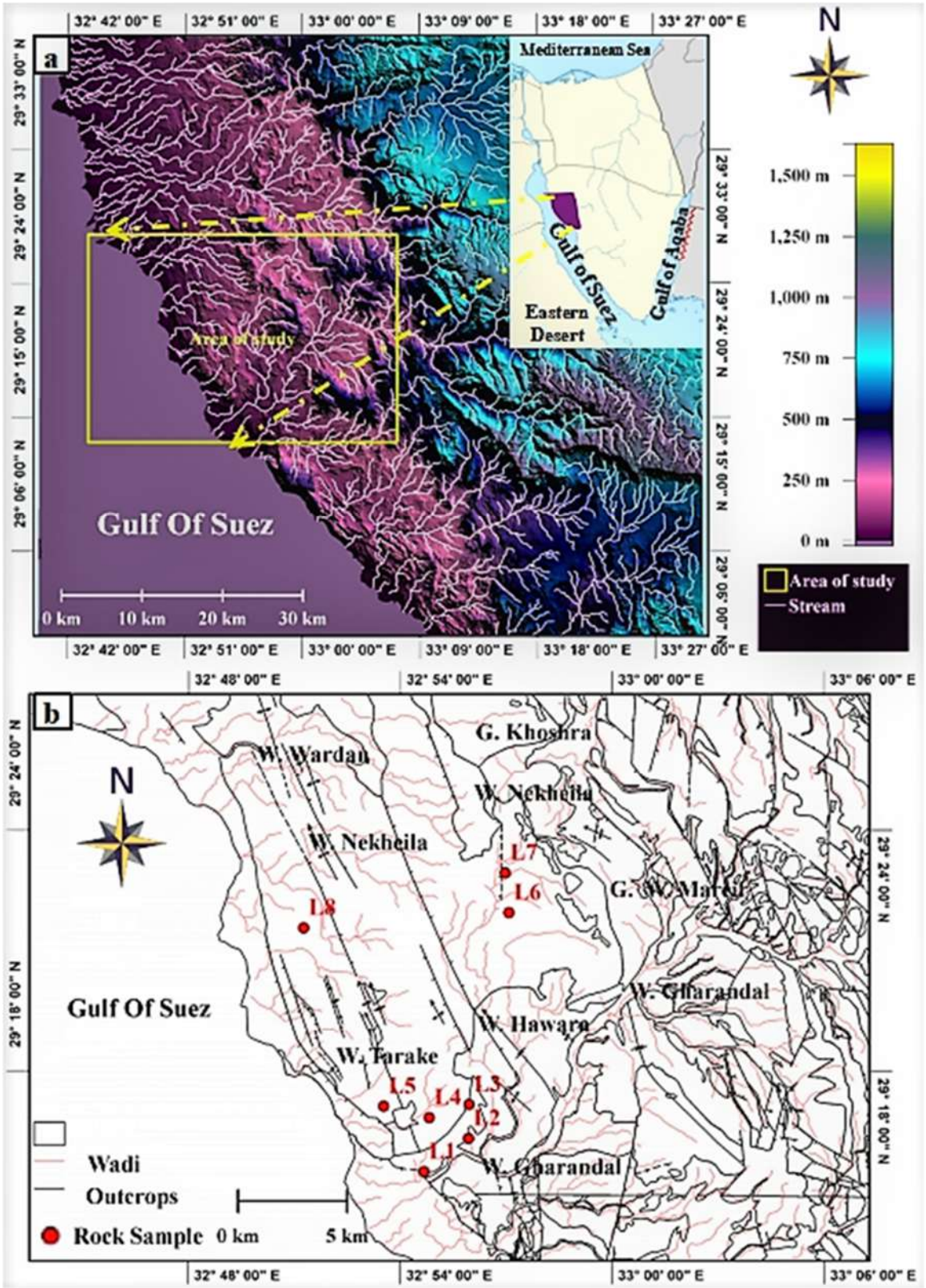

Figure1. (a) Elevation map derived from SRTM DEM images. The map shows the location of Ras Malaab area; the yellow rectangle labeled (area of study). (b) The structure map of the studied area shows the main fault trends (modified after [25]), drainage systems, and rock sample locations (L(1-8), Wadi Nekheila, and G. Khoshra) in area of study. N.B.: G = Gebel, W = Wadi.

In the area of study, Gharandal mega-sequence deposition was terminated by pre-Balayim event [33]. Rift-bounding faults movements were positively inverted due to movement along the Dead Sea transform [34], and the Gulf of Suez became a semi-closed basin [35]. However,

negative inversion rejuvenated the rift-bounding faults. Ras Malaab mega-sequence was laid down during these pre-Balayim positive inversion [34], and recovered rifting confined to the rift shoulders and onshore parts [8]. Precipitation of lowstand salt and anhydrite mark the beginning of Ras Malaab mega-sequence [35]. Middle Miocene Balayim formation of alternating limestone and evaporites [36] reflects increased rift activity. Late Miocene South Gharib formation of offshore halite layers-onshore evaporites represents maximum rifting rate of Ras Malaab Mega-sequence rift pulse [15]. Late Miocene Zeit Formation of offshore marl-halite interbeds-onshore evaporites reflects slowing down of rift tectonics activity at the close of Miocene, which seized Ras Malaab mega-sequence in offshore Gulf of Suez areas but onshore areas were still being uplifted. Pliocene-Recent Clastics and evaporites were laid down later in offshore sub-basins [37].

The evaporites in the present study belong to Ras Malaab mega-sequence. They were deposited during the middle-late Miocene pulse of the Gulf of Suez Rift. These evaporites were deposited in onshore sub-basins on the eastern coast of the Suez Gulf. These sub-basins received calcium sulphate/carbonate rich water influx that restocked the brine; as a result, the main deposits in the area under study are mappable gypsum layers of tens of meters in thickness interrupted with carbonate inter-laminations of millimeters in thickness (Figure 2).

3. Datasets and Methodology

The evaporite facies were identified by analyzing ASTER images (L1B: scene number AST_L1T_15735, taken in July 2001), Landsat 8 (AOL: scene number LC08_L1TP_175040, taken in August 2020), and SRTM DEM images (n29_e032_1arc_v3 and n29_e033_1arc_v3, taken in August 2005) in multiple stages of pre-processing and processing. We obtained the necessary ASTER and SRTM scenes (Figure 3) from the Earthdata website operated by NASA (National Aeronautics and Space Administration) and the Landsat scenes (Figure 3) from the GLOVIS website operated by USGS (United States Geological Survey) and Earth Explorer website operated by NASA. All scenes are geo-referenced to UTM Zone 36N and WGS-84 datum. To process the images, we used Envi Imagine (versions 5.1 and 4.8), and we created a facies outcrops map using Arc GIS (version 10.4.1). We studied thin sections of rock samples under a transmitting light microscope to identify the twenty-two different mineralogic varieties. The sample location numbers and lithologic logs (Figure 2) were used to supervise image classifications. In a previous study [8], the stratigraphic succession of Ras Malaab evaporites was examined in eight different locations within the present studied area (L1:8, Figure 1b).

3.1. ASTER images for analysis

To prepare ASTER images for analysis (as shown in Figure 3), several steps were taken. Firstly, radiometric calibration was carried out on the VNIR (visible and near-infrared), SWIR (short wave infrared), and TIR (thermal infrared) bands. This was done using the Envi built-in radiometric calibration function, which takes into account factors such as reflectance calibration, atmospheric transmittance, and other surface image elements [38]. The measurements obtained were then input into a Gauss-Seidel iteration radiative transfer code to predict atmosphere radiance [39]. The predicted radiances were compared with the digital numbers reported by the sensor to obtain radiometric calibration [38]. Secondly, the wavelengths of all image bands were adjusted to their respective central wavelength values using the Edit Envi Header tool [40]. Thirdly, atmospheric correction was applied to the VNIR and SWIR bands using Quick atmospheric correction, while Thermal atmospheric correction was applied to the TIR bands. This step helped to obtain more accurate surface reflectance and improved the extraction of surface parameters from the images [40, 41]. Fourthly, all the image bands were stacked, and the images were resampled to a spatial resolution of 30 m. Finally, pan-sharpening was applied to the images using the Envi built-in pan-sharpening function PCA. The principal component (PC) image with major variance and information was replaced by a panchromatic image, making it suitable for images with any number of bands [42].

To prepare Landsat 8 (AOL) images for analysis (shown in Figure 3), we followed a three-step process. First, we applied atmospheric correction to the VNIR and SWIR bands and thermal atmospheric correction to the TIR bands, using a quick method [40]. Secondly, we stacked all bands and adjusted the image's spatial resolution to 15 m. Finally, we pan-sharpened the images to principal components using bilinear method [42].

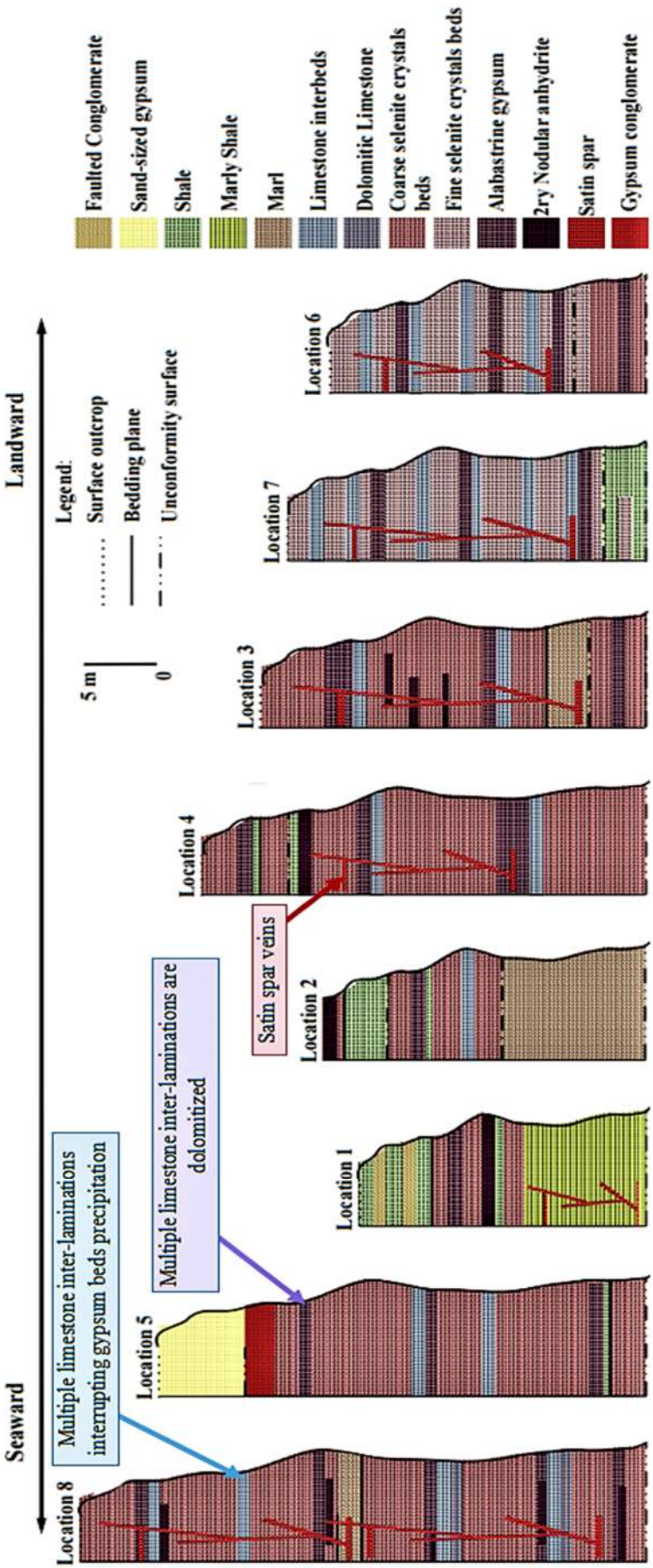

Figure 2. Lithologic logs of rock sample locations in the area of study (Modified after [8]).

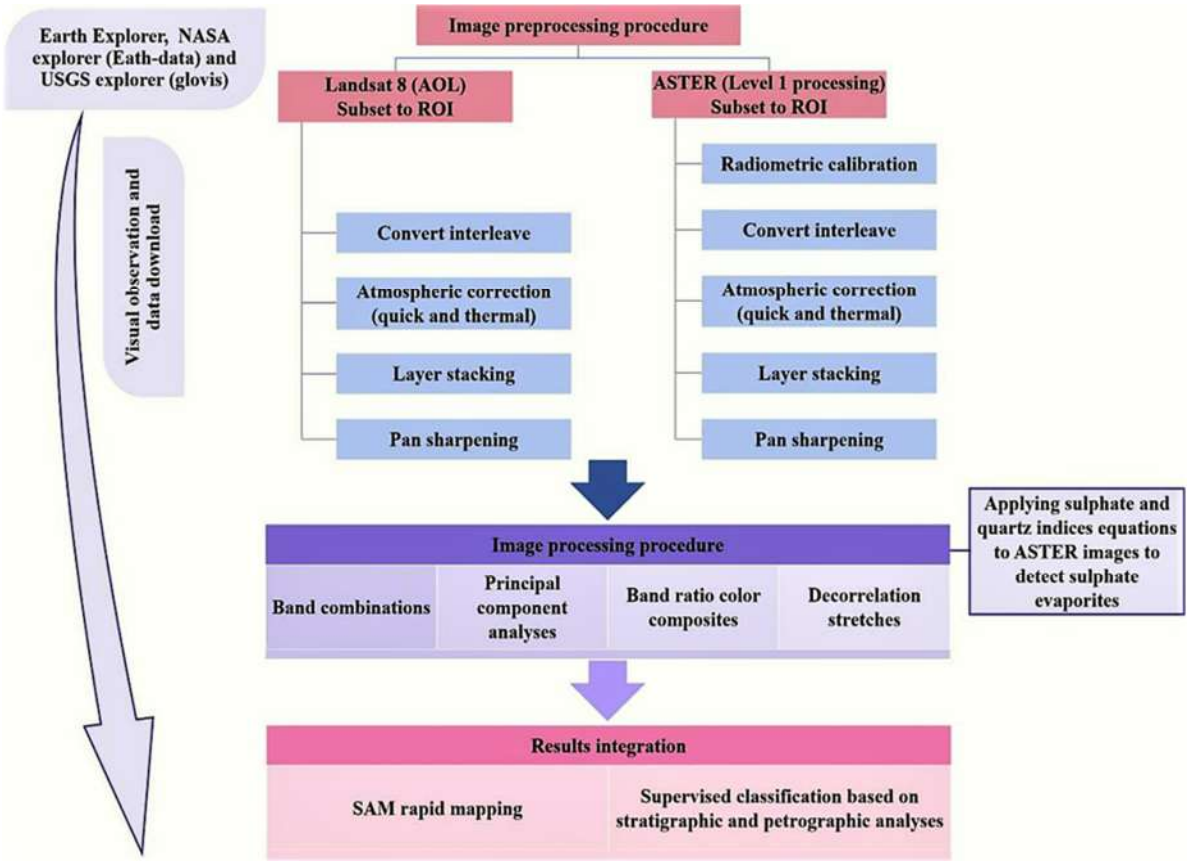

Figure 3. Chart showing the workflow used in the current study.

3.2. Processing of ASTER and Landsat images (Figure 4)

We analyzed ASTER and Landsat images (Figure 3) using VNIR-SWIR band combinations, ratios, and principal components. These methods are effective in identifying evaporites, especially gypsum, due to its molecular water interactions with these wavelengths [6]. Previous studies have successfully used SWIR and TIR wavelengths, along with mineral index equations, to map various lithologies. In our study, we utilized quartz and sulphate indices [6]: gypsum appears as white patches on applying the sulphate index and black patches on applying the quartz index. Gypsum also behaves differently in the TIR region than in its surroundings, making it easier to detect by adding TIR bands to composites and calculated indices [6]. To separate different facies, we utilized various ASTER and Landsat RGB false composites suitable for the facies under study.

3.2.1. Sulphate index (SI) and quartz index (QI)

There are established and commonly used indices that use image transformation to accurately identify gypsum facies in their surrounding areas [6]. The Sulphate Index (SI) and Quartz Index (QI) were calculated by using thermal infrared ASTER bands 10, 11, and 12.

$$SI = \frac{(band10) \times (band12)}{(band11) \times (band11)} \quad [6] \quad \text{(Figure 4a)}$$

$$QI = \frac{(band11) \times (band11)}{(band10) \times (band12)} \quad [43] \quad \text{(Figure 4b)}$$

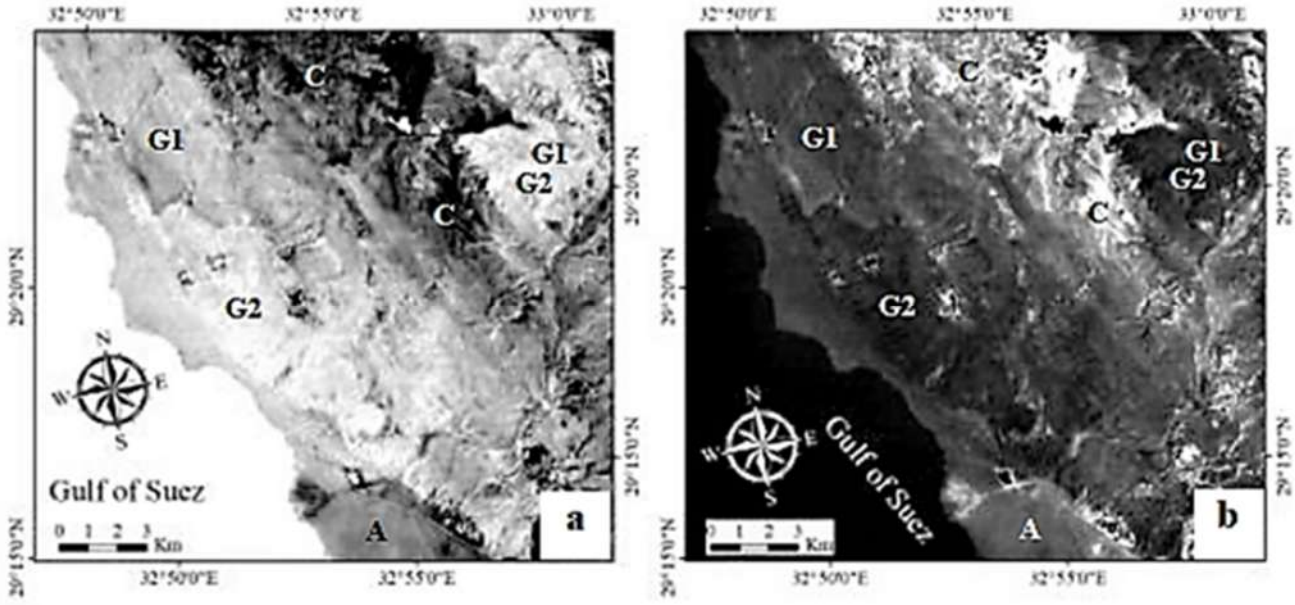

Figure 4. ASTER images mineral indices and band combinations. (a) ASTER band SI (evaporites are light patches) [6]. (b) ASTER band QI (evaporites are dark patches) [43]. N.B.: G1 = Primary Gypsum, G2 = Secondary Gypsum, C = Carbonates, A = Alluvium.

3.2.2. Spectral signature analysis (Figures 5 and 6)

Spectral signatures of the different gypsum/carbonate types in the area of study were analyzed. The spectral signature is unique for each mineral; it shows the spectral band reflectance for each mineral. Mineral alterations like dehydration, recrystallization, impurity content, primary/secondary mineral generations, crystal growth mode, … etc. These changes are generally detected in the mineral spectral signature. The main observed minerals in the studied area are primary/secondary/tertiary gypsum, secondary anhydrite, calcium, and magnesium carbonates. The spectral signatures of these minerals were studied by many authors. Moreover, these authors derived mineral indices based on the spectral signatures of the minerals, where the reflectance values of highly reflected spectral bands for each mineral are divided by the least reflected band values or the highly absorbed. Gypsum has high reflectance values at ASTER bands 4 and 8, while bands 6 and 9 are highly absorbed [6]; anhydrite highly reflects all ASTER bands but absorbs bands 6 and 9 [44]; calcite reflects bands 6 and 9 but absorbs band 8 [45], and Dolomite reflects bands 6 and 8 but absorbs band 7 [46]. In the area of study, the main rock composition is gypsum, and it is observed in two forms, which are massive coarse crystalline gypsum with minor calcite micrite laminae, and bedded fine crystalline gypsum with numerous calcite micrite laminae. Petrographic studies show that many parts of the gypsum-micrite sequence are altered into secondary minerals and textures. At scarce parts, gypsum is completely dehydrated into nodular anhydrite and anhydrite pseudomorphs after swallow-tail selenite. But most commonly gypsum is partially dehydrated into alabaster and gypsum with prismatic anhydrite inclusions. Micrite is formerly composed of mud-sized calcite crystals; it recrystallizes at early diagenetic stages into coarser (sand-mud sized) dolomite and at later diagenetic stages, micrite remnants, and dolomite recrystallize into sand-sized drusy pure calcite crystals. Moreover, some anhydrite crystals are replaced by drusy calcite, and some parts of drusy calcite are replaced by karst gypsum. Each of these sulphate-carbonate mineral generations shows a distinct spectral signature (Figures 5 and 6), and some spectral signatures show intermediate characteristics between carbonates and sulphates, which indicate transition and mixing. Moreover, grain/crystal size, mineral genesis, inter-crystalline impurities and tectonic structures disturb the spectral signatures of minerals (Figures 5 and 6).

The spectral signatures of the gypsum mineral generations under study lie in the range of SWIR bands, where gypsum absorbs most VNIR radiations, reflects different SWIR radiations but absorbs the others, and has a very outstanding reaction with TIR bands due to its molecular water overtones. As a result, different false colour composites were used in the present study to separate the mineral generations and varieties in

the studied area based on the spectral signatures of the lithologic/mineralogic composition in the area (Figures 5 and 6). The false color composites were created by applying band combinations, principal component composites, and band ratio composites, where the composites were created as (False Color Composite Images RGB VNIR-SWIR-TIR, SWIR or SWIR-TIR) band combination.

In the studied area, the unique spectral signatures of different gypsum/carbonate types were analyzed to determine their mineral composition. Each mineral has a distinct spectral signature that shows its spectral band reflectance. Mineral alterations such as dehydration, recrystallization, and impurity content can be detected in the spectral signature. The main minerals observed in the area are primary/secondary/tertiary gypsum, secondary anhydrite, calcium, and magnesium carbonates. Many authors have studied the spectral signatures of these minerals and derived mineral indices based on their reflectance values. Gypsum has high reflectance values at ASTER bands 4 and 8, while anhydrite highly reflects all ASTER bands but absorbs bands 6 and 9. Calcite reflects bands 6 and 9 but absorbs band 8, and dolomite reflects bands 6 and 8 but absorbs band 7.

In the area of study, the main rock composition is gypsum, observed in two forms: massive coarse crystalline gypsum with minor calcite micrite laminae and bedded fine crystalline gypsum with numerous calcite micrite laminae. Petrographic studies show that many parts of the gypsum-micrite sequence are altered into secondary minerals and textures, and gypsum is partially dehydrated into alabaster and selenite with prismatic anhydrite inclusions. Each sulphate-carbonate mineral generation shows a distinct spectral signature, indicating transition and mixing.

False color composites were used in the present study to separate the mineral generations and varieties in the studied area based on the spectral signatures of the lithologic/mineralogic composition. The spectral signatures of the gypsum mineral generations under study lie in the range of SWIR bands, with gypsum absorbing most VNIR radiations and reflecting different SWIR radiations but absorbing the others. Different false color composites were created by applying band combinations, principal component composites, and band ratio composites. These composites were created as False Color Composite Images RGB VNIR-SWIR-TIR, SWIR or SWIR-TIR band combinations. Grain/crystal size, mineral genesis, inter-crystalline impurities, and tectonic structures can also affect the spectral signatures of minerals.

Band combinations

Various combinations of ASTER bands were tested, and the results are shown in Figure 7. The RGB false color combinations of 3-4-5, 4-6-8, 4-6-9, and 4-8-9 (Figures 7a:d) proved to be highly effective in distinguishing gypsum (G) from surrounding carbonates (C), clastics and alluvium (A), as well as differentiating between primary gypsum generation (G1) and secondary gypsum (G2). Another band combination of 3-8-10 (Figure 7e) was found to be very useful in separating gypsum (G) from surrounding carbonates (C), clastics and alluvium (A), and in distinguishing between primary massive gypsum generation (G1m), primary bedded gypsum generation (G1b), and secondary gypsum (G2). However, the RGB combination of 6-11-12 (Figure 7f) was only effective in separating gypsum (G) from surrounding carbonates (C), clastics, and alluvium (A). Other studies used the ASTER VNIR-SWIR composite RGB 3-4-6 to separate land cover elements of oases and forests in Xin Jiang, China [47]. Others utilized the ASTER SWIR composite RGB 4-6-8 to separate on-shore gas seep-induced alterations in London [48] and meta-basalt alteration zones in Iran [49]. Also, the ASTER TIR bands were used to create the composite RGB 12-13-5 to separate ore facies in Bulgaria [50].

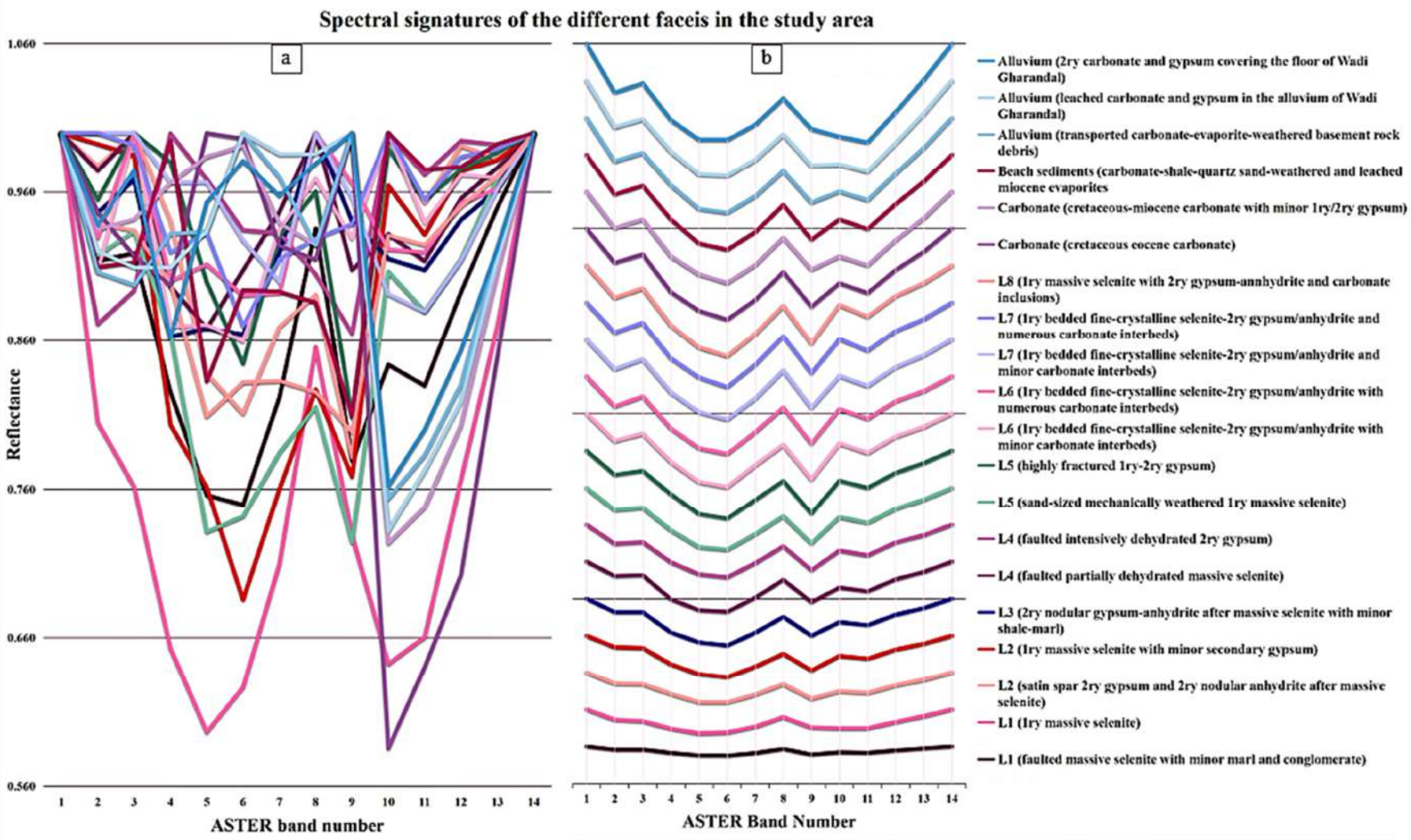

Figure 5. (a) Spectral signatures of the different mineralogic varieties in the area of study, with reference to the petrographic sample locations (L1:8), (b) Stacked spectral signatures of the mineralogic varieties.

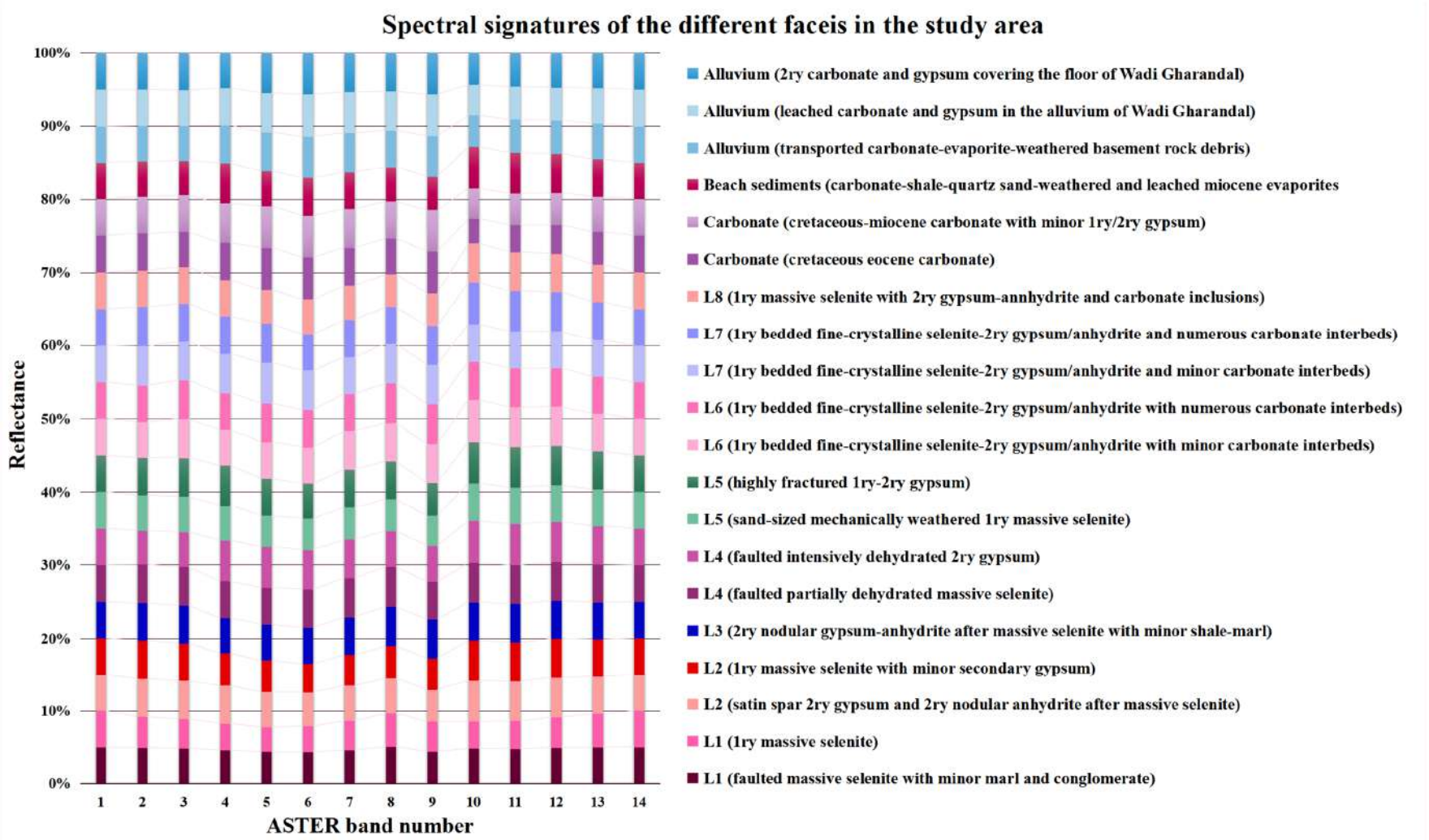

Figure 6. ASTER bands reflectance percentage of the mineralogic varieties under study.

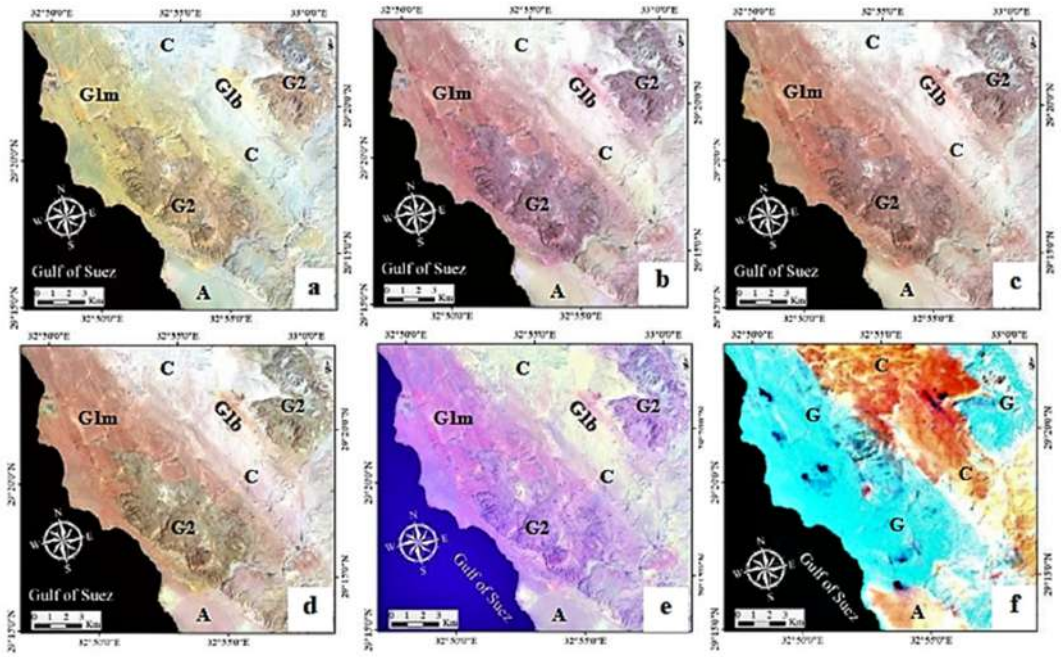

Figure 7. ASTER band combination false colour composite image RGB. (a) 3-4-5. (b) 4-6-8 [48, 49]. (c) 4-6-9. (d) 4-8-9. (e) 3-8-10. (f) 6-11-12. N.B.: G = Gypsum, G1 = Primary Gypsum, G2 = Secondary Gypsum, C = Carbonates, A = Alluvium.

Landsat false color composites (Figure 8) using various RGB combinations such as (2-3-6), (4-5-6), (3-6-11), (3-7-11), (6-7-11), and (7-9-11). These combinations were highly effective in distinguishing gypsum (G) from the surrounding carbonates (C), clastics, and alluvium (A); Figure 8 displays gypsum (G) carbonates (C), clastics, alluvium (A), primary (G1), and secondary gypsum (G2). In a study, Landsat VNIR-SWIR RGB 7-4-2 was used to map the exposed pre- and syn-rift sedimentary units at the Sidri-Feiran area of the southwestern Sinai Peninsula, Egypt [51].

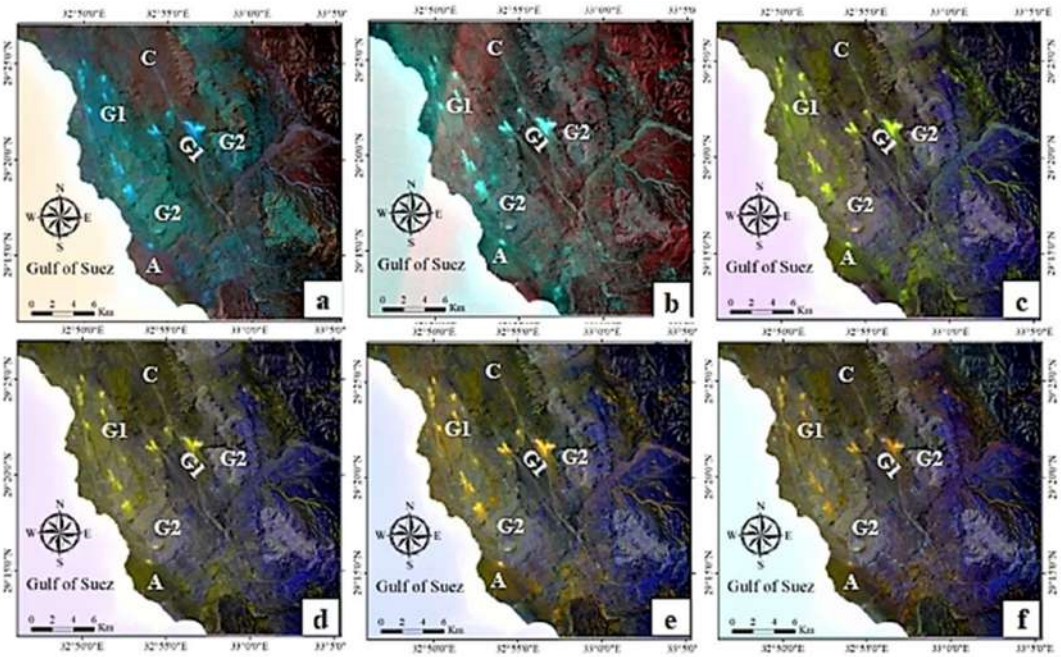

Figure 8. Landsat band combination false color composite image RGB. (a) 2-3-6. (b) 4-5-6. (c) 3-6-11. (d) 3-7-11. (e) 6-7-11. (f) 7-9-11. N.B.: G1 = Primary Gypsum, G2 = Secondary Gypsum, C = Carbonates, A = Alluvium.

3.2.3. Principal component analysis PCA

This technique enhances the spectral features of rocks and minerals on the surface by reducing the effects of irradiance [52]. Various analyses were conducted using ASTER and Landsat principal components. Figure 9 shows ASTER PC false color composites. RGB PC 3-4-9, PC 4-6-8, PC 4-8-9, PC 3-6-10, PC 3-8-10, and PC 9-11-12 were highly effective in distinguishing gypsum (G) from carbonates (C) and also in differentiating between primary gypsum generation (G1), secondary gypsum (G2), faulting, brecciation, and alteration of gypsum at fault scarps (F). Nevertheless, RGB PC 4-8-9 (Figure 9c) and PC 9-11-12 (Figure 9f) were the most effective false color composites as they separated carbonates, primary gypsum, secondary gypsum, and alluvium. In addition, these false composites distinguished between massive and bedded primary gypsum (G1m) and (G1b), respectively, and RGB PC 9-11-12 (Figure 9f) could identify anhydrite (An) as well. In other studies, ASTER VNIR-SWIR RGB PC 2-4-6 was used to map lithologies in Atlas Mountains in Morocco [53], whereas ASTER RGB PC 8-5-2, 4-6-7, 4-5-7 were used to map gold mineralization in Central Alborz, Iran [54].

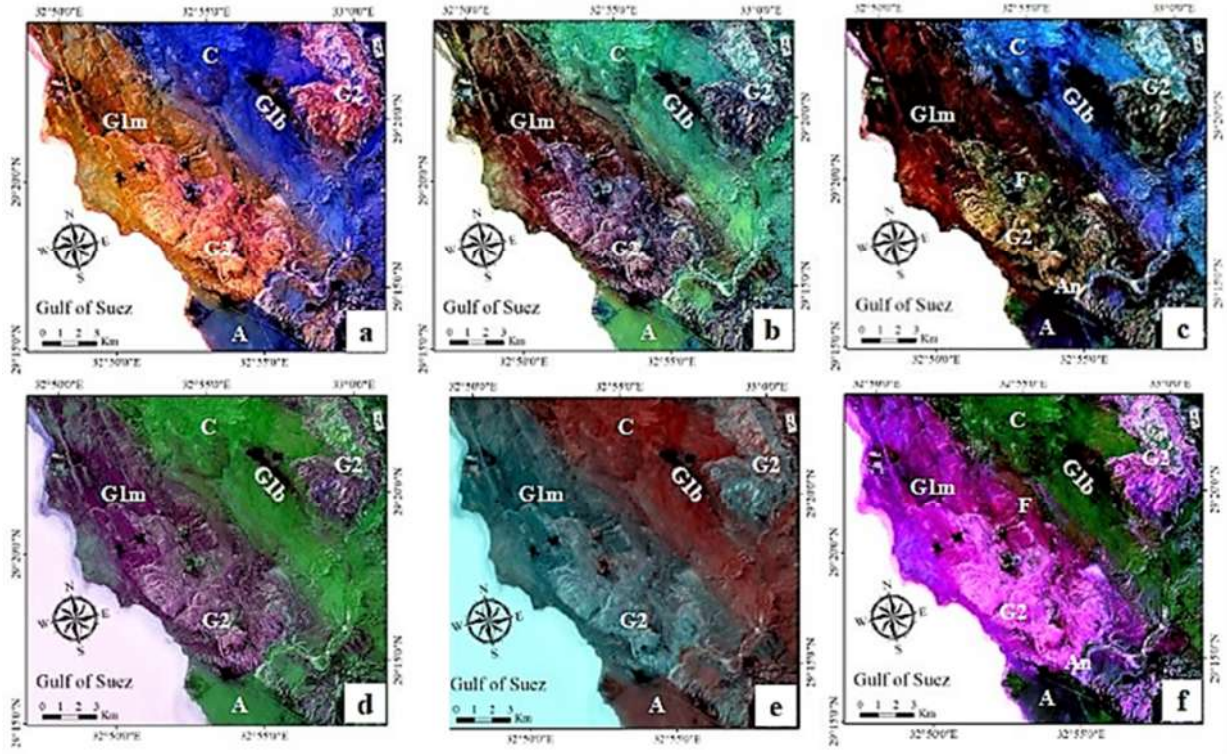

Figure 9. Aster principal component band combinations False color composite image RGB. (a) PC 3-4-9. (b) PC 4-6-8. (c) PC 4-8-9. (d) PC 3-6-10. (e) PC 3-8-10. (f) PC 9-11-12. N.B.: G1m = Primary Massive Gypsum, G1b = Primary Bedded Gypsum, G2 = Secondary Gypsum, F = Faulted, Brecciated and Altered Gypsum, C = Carbonates, An = Anhydrite, A = Alluvium.

In Figure 10, Landsat PC false color composites are presented. RGB Combinations of PC 1-2-3, PC 4-5-6, PC 4-6-7, and PC 6-7-10 (Figures 10a-d) were highly effective in differentiating gypsum (G) from the surrounding carbonates (C), clastics, and alluvium (A). They also distinguished between primary massive gypsum generation (G1m), primary bedded gypsum generation (G1b), and secondary gypsum (G2). Additionally, false color composites RGB PC 4-5-6, PC 4-6-7, and PC 6-7-10 (Figures 10b-d) revealed the various carbonate-gypsum replacement halos, gypsum dehydration halos, and its transformation to anhydrite (An). Furthermore, they clarified faulting, brecciation, and alteration of gypsum at fault scarps (F). These false color composites captured the minerals transition halos (H).

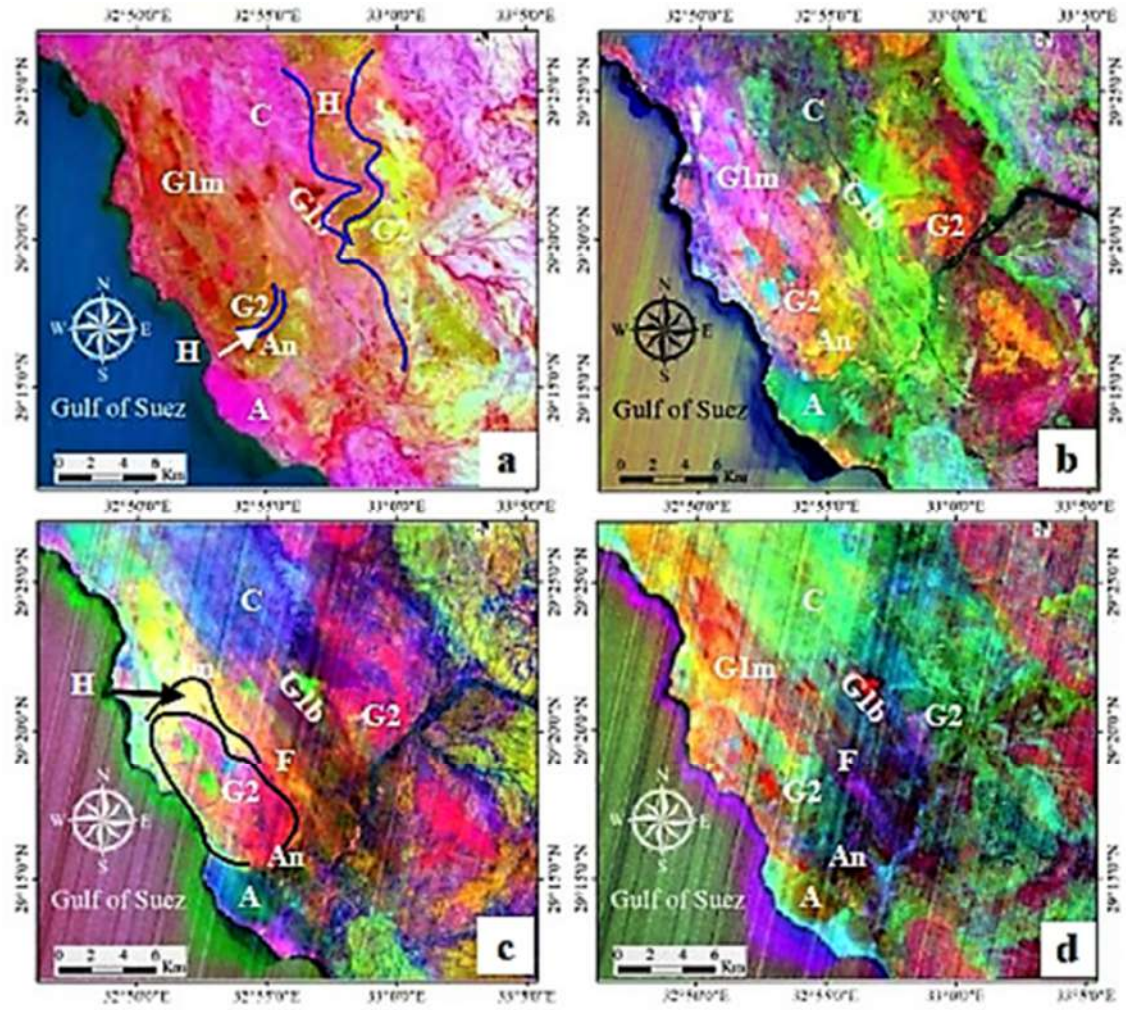

Figure 10. Landsat principal component band combinations False color composite image RGB. (a) PC 1-2-3. (b) PC 4-5-6. (c) PC 4-6-7. (d) PC 6-7-10. N.B.: G1m = Primary Massive Gypsum, G1b = Primary Bedded Gypsum, G2 = Secondary Gypsum, F = Faulted, Brecciated, and Altered Gypsum, An = Anhydrite, C = Carbonates, A = Alluvium, H = Mineral transition halos and gradational contacts.

3.2.4. Band ratios

The application of band ratios involved dividing reflective bands by absorptive bands [52]. Various ASTER and Landsat Band ratios were utilized, with the ASTER band ratios and ratio false color composites displayed in Figure 11. Ratios 4/6, 4/9, 8/6, and 8/9 (Figures 11a:d) were effective in revealing the different alteration gypsum halos. The false color composite images RGB ratio 4/6-4/9-8/6, ratio 4/6-4/9-8/9, ratio 4/6-8/6-8/9, and ratio 4/9-8/6-8/9 (Figures 11e:h) were particularly useful in distinguishing between primary gypsum generation (G1) and secondary gypsum (G2), carbonates (C), alluvium (A), and anhydrite (An). As well as determining massive (G1m), bedded (G1b), and faulted (F) primary selenite. In 1999, gypsum facies were successfully identified using the ASTER SWIR band ratio (4+8) reflectance / (6+9) absorption [52].

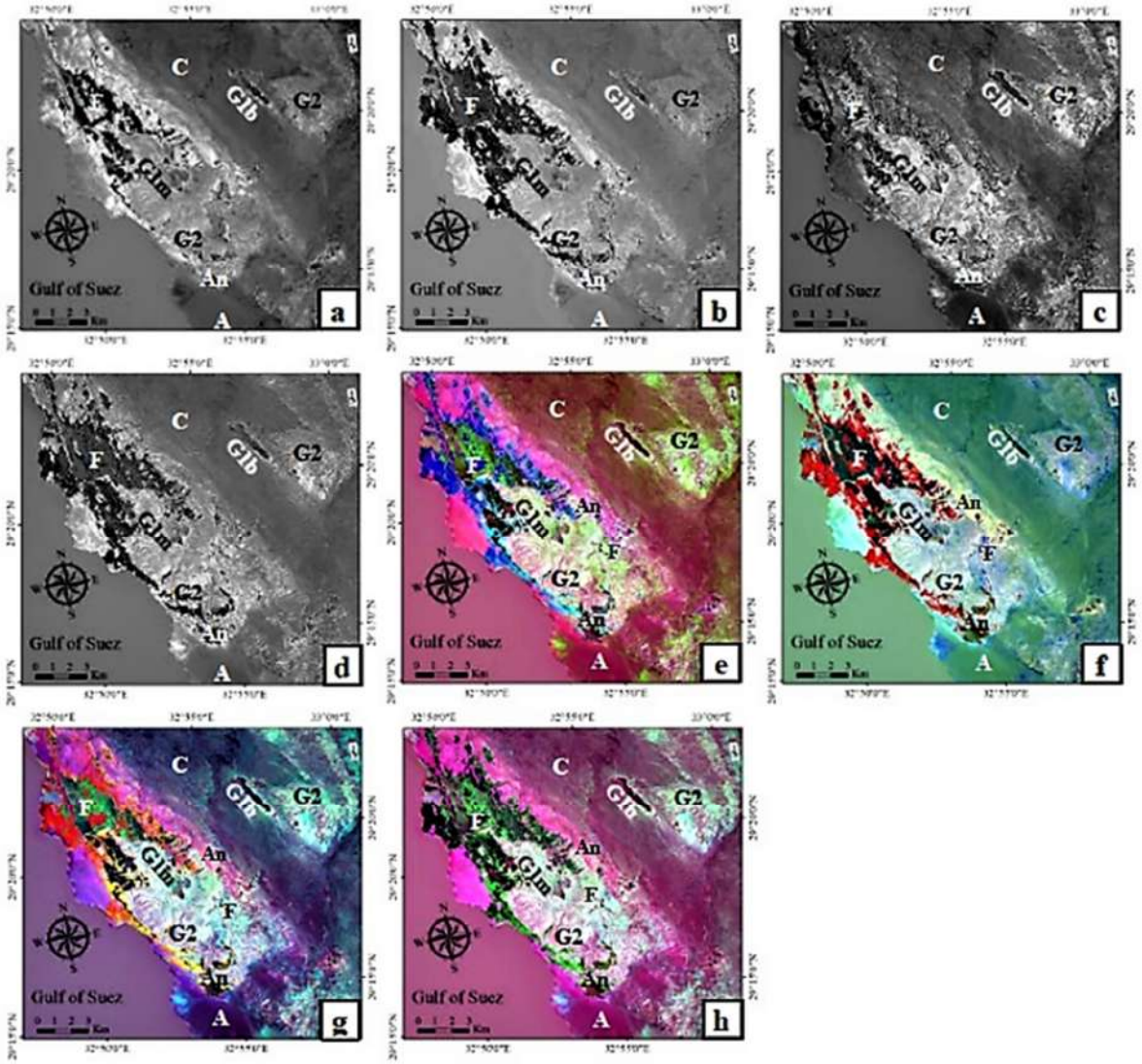

Figure 11. Aster band ratio combinations. ASTER band Ratio image (a) 4/6 [52]. (b) 4/9 [52]. (c) 8/6 [52]. (d) 8/9 [52]. False color composite image RGB (e) Ratio 4/6-4/9-8/6. (f) Ratio 4/6-4/9-8/9. (g) Ratio 4/6-8/6-8/9. (h) Ratio 4/9-8/6-8/9. N.B.: G1 = Primary Gypsum, G2 = Secondary Gypsum, F = Faulted, Brecciated and Altered Gypsum, C = Carbonates, A = Alluvium.

Figure 12 displays Landsat band ratios and ratio false color composites. Band ratios 7/2, 7/5, 7/6, 7/8, and 7/11 (Figures 12a-e) were effective in distinguishing gypsum from surrounding carbonates and alluvium. The false color composite images RGB ratio 7/2-7/5-7/6, ratio 7/2-7/5-7/8, and ratio 7/2-7/5-7/11 (Figures 12f:h) were very useful in separating gypsum (G) from carbonates (C) and alluvium (A), and distinguishing between primary gypsum generation (G1) and secondary gypsum (G2). Another study in 2017 used Landsat VNIR-SWIR band ratios 6/4, 6/2, 7/6, 4/6, 4/2, and 6/7, as well as false color composites of these ratios to map different facies in Biga Peninsula, Turkey [55].

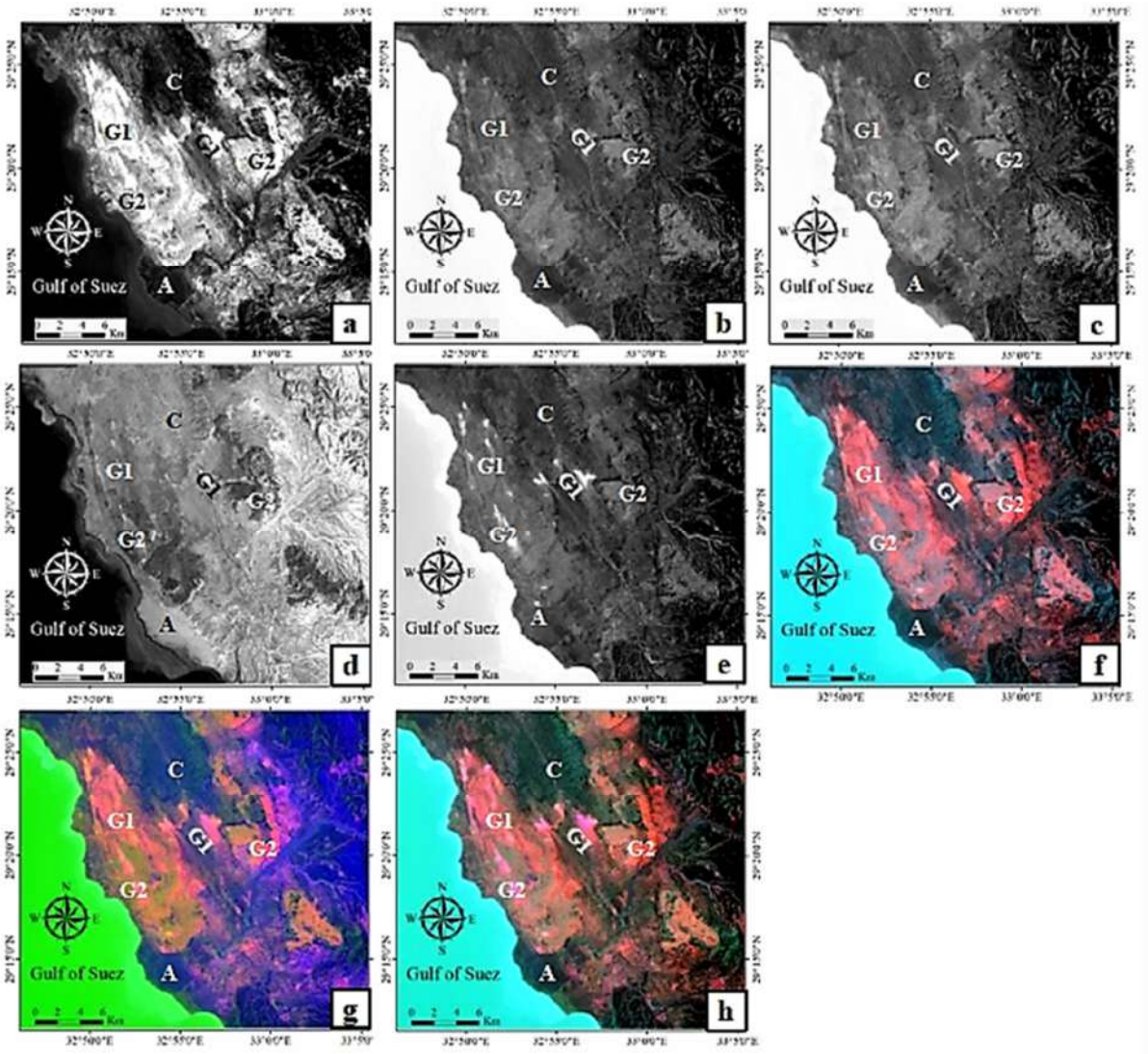

Figure 12. Landsat band ratio combinations. Landsat band ratio (a) 7/2. (b) 7/5. (c) 7/6. (d) 7/8. (e) 7/11. False color composite RGB (f) Ratio 7/2-7/5-7/6. (g) Ratio 7/2-7/5-7/8. (h) Ratio 7/2-7/5-7/11. N.B.: G1 = primary gypsum, G2 = secondary gypsum, C = carbonates, A = alluvium.

3.2.5. Decorrelation stretches

Transformed color composite images were created by selecting certain spectral bands through the principal component transformation of images. These images were then subjected to decorrelation stretches that enhanced their contrast and primary colors [56]. After contrast enhancement, the principal component images were transformed back to their original form for display [57]. Different images from ASTER and Landsat Decorrelation stretches were produced (Figures 13 and 14).

The ASTER Decorrelation stretch color composites RGB 3-4-8, DS 4-6-8, and 4-8-9 (Figures 13a-c) are particularly effective in distinguishing between primary gypsum generation (G1), faulted and altered primary gypsum (F), secondary gypsum (G2), anhydrite (An), alluvium (A), and the surrounding carbonates (C). In 2016, A study used ASTER SWIR RGB DS 4-9-8 to map evaporites and carbonate outcrops along the Salt Lake Fault in Turkey [58], while another study in 2020 used ASTER SWIR RGB DS 4-6-8 in 2020 to map evaporites of Kohat plateau in Pakistan [59].

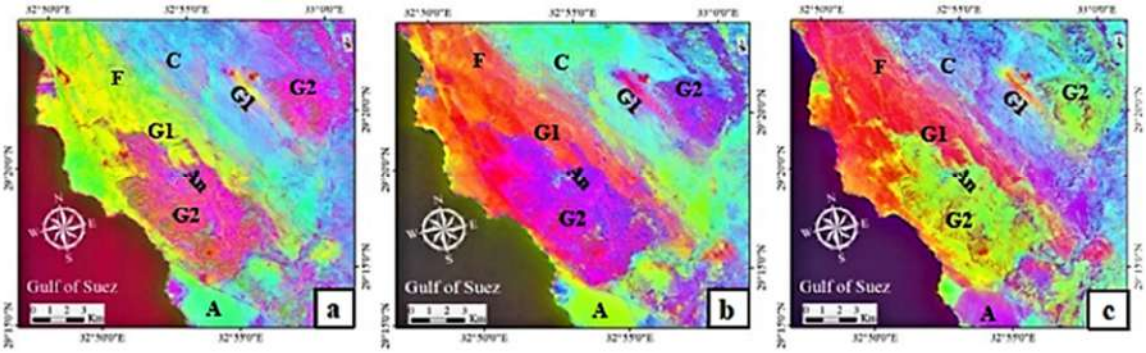

Figure 13. Aster decorrelation stretch band combinations False colour composite image RGB. (a) DS 3-4-8. (b) DS 4-6-8 [59]. (c) DS 4-8-9 (modified from RGB DS 4-9-8 [58]). N.B.: G1 = primary gypsum, G2 = secondary gypsum, An = anhydrite, C = carbonates, A = alluvium.

Figure 14 displays Landsat Decorrelation stretch color composites. The false color composite RGB DS 5-6-7 and DS 7-8-11 shown in Figures 14a and 14b proved to be highly efficient in distinguishing between gypsum (G), carbonates (C), and alluvium (A) as well as identifying primary gypsum generation (G1), secondary gypsum (G2), and anhydrite (An).

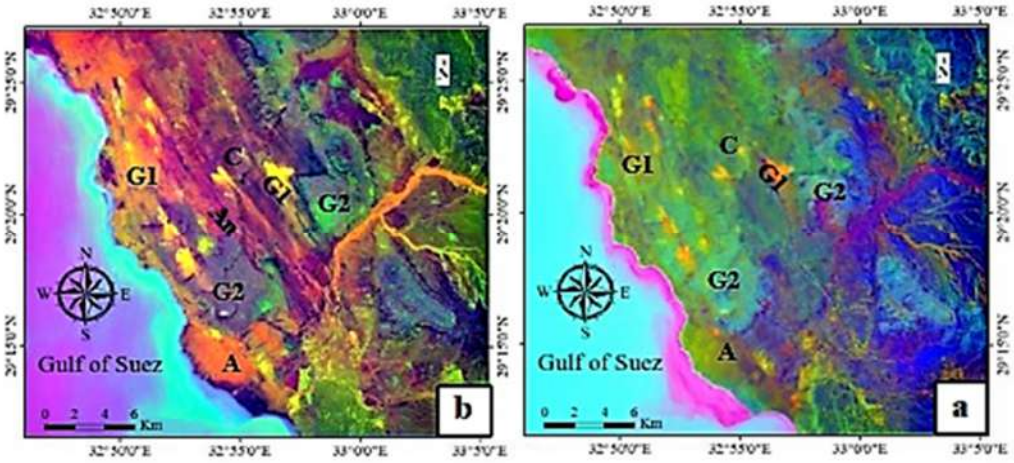

Figure 14. Landsat decorrelation stretch band combinations False color composite RGB. (a) DS 5-6-7. (b) DS 7-8-11. N.B.: G = gypsum, G1 = primary gypsum, G1m = primary massive gypsum, G1b = primary bedded gypsum, G2 = secondary gypsum, An = anhydrite, C = carbonates, A = alluvium.

3.2.6. SAM rapid mapping (Figures 15a and 15b)

The SAM rapid mapping technique utilizes spectral similarity to compare image spectra to reference spectra. These reference spectra can be obtained from laboratory spectra, field spectra or extracted from the image itself. In this study, the reference spectra were extracted from ASTER and Landsat 8 images. The Envi built-in SAM function was used to measure the spectral similarity between the two sets of spectra by calculating the angle between them. The 2D product image was treated as a vector in 3D space with the third dimension equal to the number of bands. SAM compares image pixels to given spectral classes and produces a value ranging from zero (low resemblance) to one (high resemblance) [60]. The SAM algorithm is advantageous because it is easy to use, rapid, and powerful for feature classification [61]. Therefore, it has been used by many authors in lithological discrimination and to map sedimentary facies at different locations [54, 60, 61, 62].

In order to create a facies map, supervised classification was utilized on both ASTER and Landsat images. The classification was based on the spectral properties observed in the gypsum-evaporite facies being studied, as well as the lithostratigraphic sequence of these facies (as shown in Figure 3). The classification results were stored in a shapefile, which was then used to generate the facies map in Arc GIS (Figures 16 and 17).

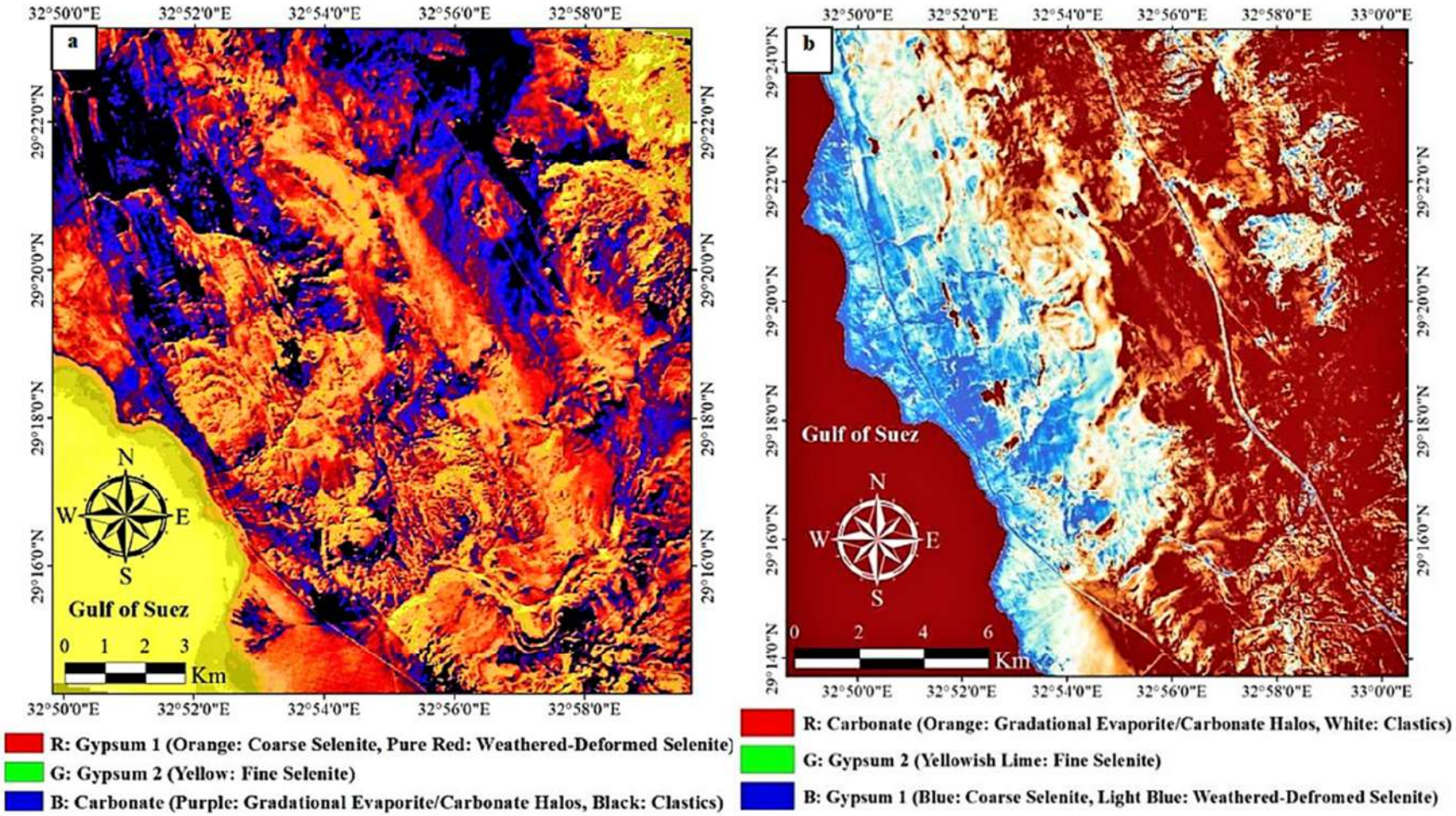

Figure 15. (a) Evaporite mapping by SAM method using ASTER images. (b) Evaporite mapping by SAM method using Landsat images.

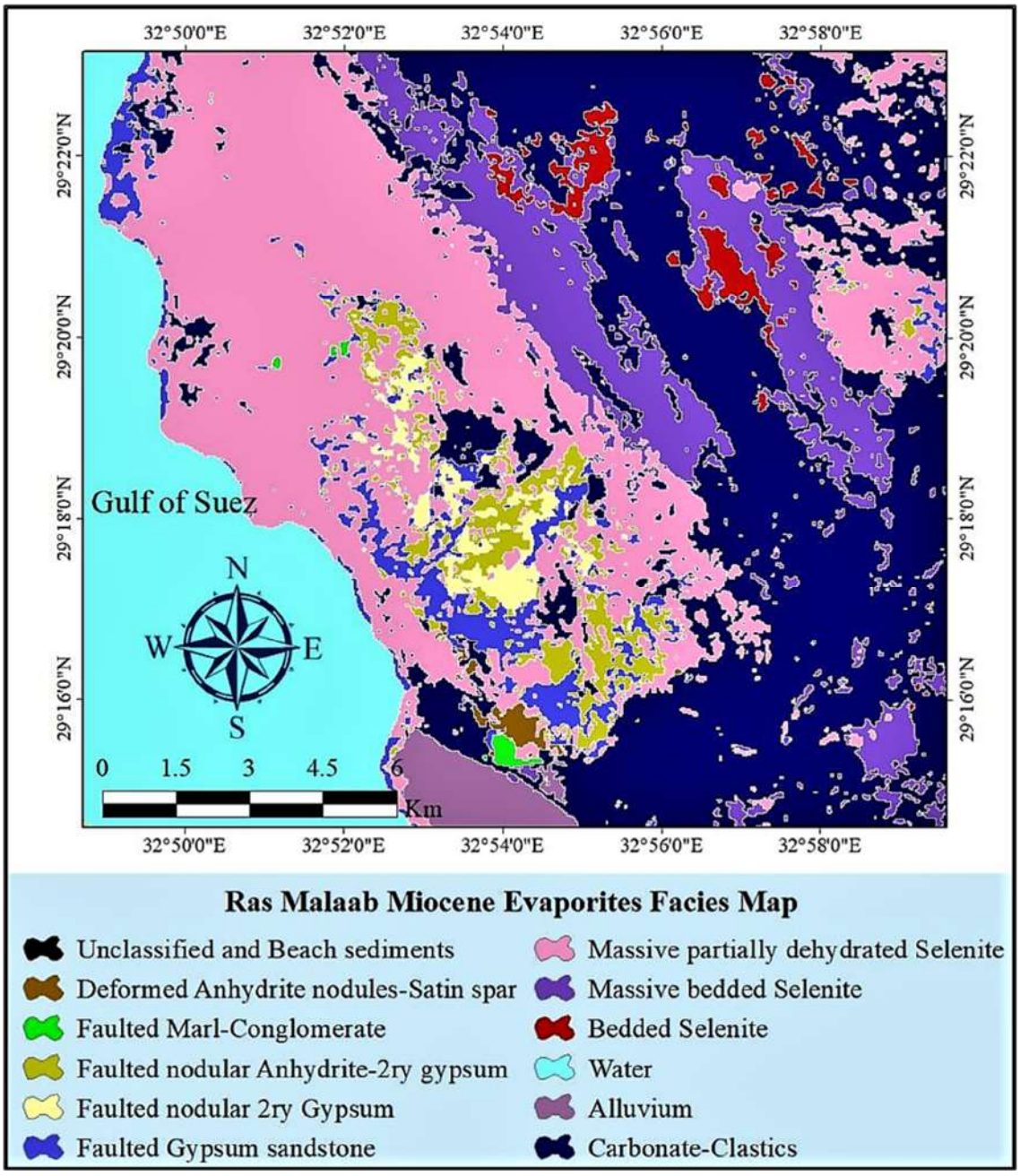

Figure 16. Facies map derived from Aster images.

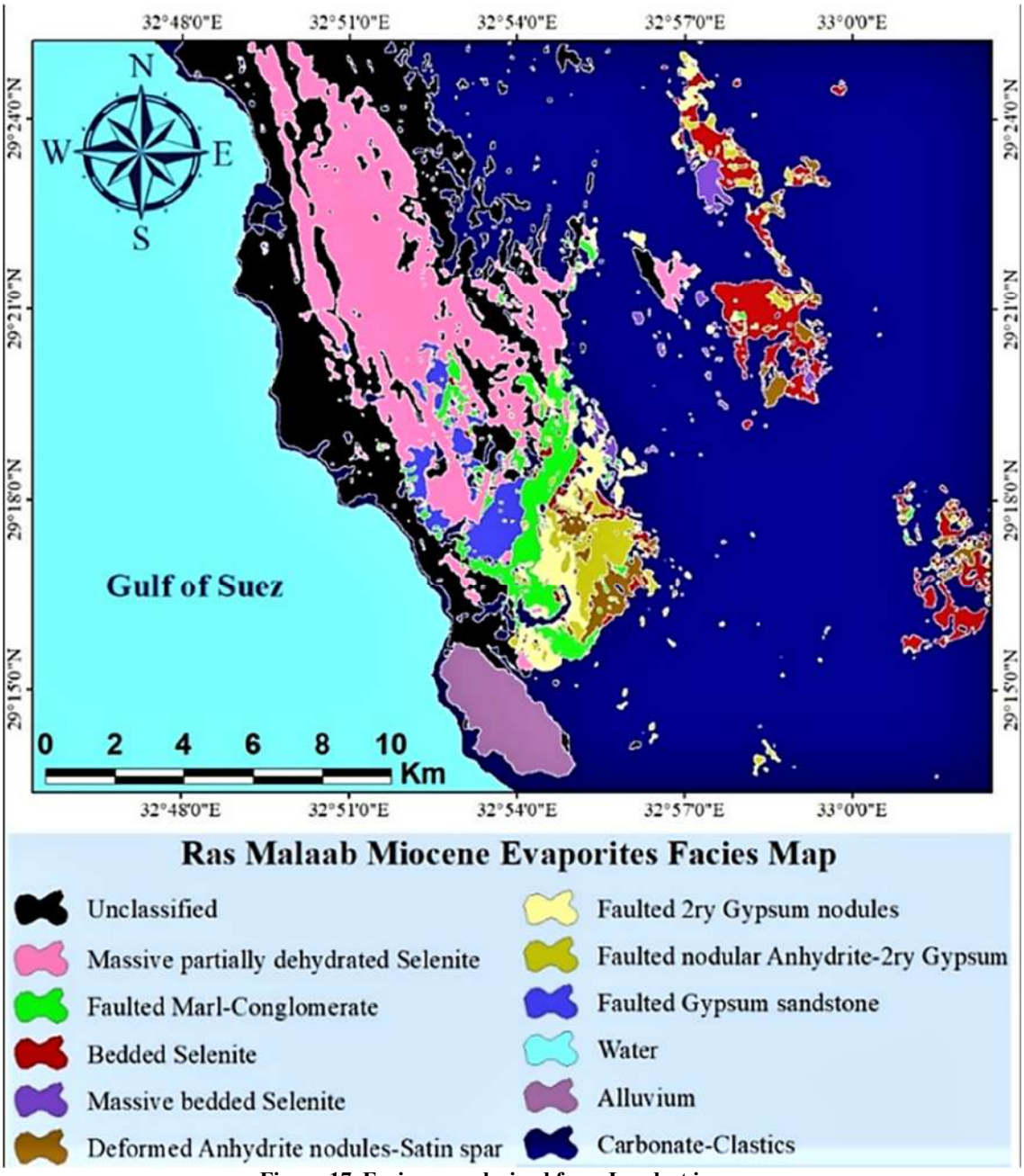

Figure 17. Facies map derived from Landsat images.

4. Conclusions

The use of ASTER and Landsat images is an effective way to map different types of rock. ASTER images provide reliable information due to their spectral data, which is more extensive than that of Landsat images. However, Landsat images have a sharper and more accurate spatial resolution, making them better for mapping geomorphologic features. Despite this, field, litho- and bio-stratigraphic, and petrographic studies are crucial to understanding the geological history of stratigraphic succession. These studies provide more detailed information about stratigraphic units that may be missed in remotely sensed data and accurate facies details that reflect the conditions at the time of rock formation.

In this study, band combinations were used to separate sulphate evaporites from pre-Miocene carbonates. False color composites of SWIR and TIR bands were the most effective in separating the two rock units, while VNIR bands were not helpful. Principal component analyses further verified and clarified the obtained results from

band combinations, in addition to showing weathered halos of gypsum (faulted, dehydrated, and/or secondary). Band ratios were effective in discriminating between carbonates, primary gypsum, secondary/dehydrated gypsum and/or secondary anhydrite. False color composites of different band ratios further separated the facies into coloured regions. Decorrelation stretch was used to separate primary massive and bedded gypsum, secondary gypsum, faulted gypsum, anhydrite, and carbonates, as well as alluvium in the study area. Dolomite in the area of study was not observed in any image although it was observed on petrographic studies. It can be concluded that it occurs as crystalline inclusions in the studied gypsum-micrite sequence, but dolomite does not occur as a separate facies or mappable rock unit. The remote sensing tools help geologists navigate and sample their studied area easily before conducting detailed studies.

References

[1]. Warren, J. (2016). Evaporites: A Geological Compendium. 2nd edition, Springer Internal Publication Switzerland, 1813.

[2]. El-Kammar, A., Surour, A., El-Sharkawi, M., & Khozyem, H. (2020). Mineral Resources in Egypt (II): Non- metallic Ore Deposits In Hamimi, Z. et al. The Geology of Egypt. Springer, USA, 589-634.

[3]. Said, R. (1990). The geology of Egypt. 1st edition, Taylor and Francis international publication, London, 734.

[4]. Pandey, S. (1985). Principles and applications of photogeology. John Wiley and Sons, 366.

[5]. Nguyen, N. (2010). Estimation of Above Ground Biomass In Tropical Forest Using Sar Data- A Case Study In Afram Headwaters Forest, Ghana, International Institute for Geo-information Science and Earth Observation. Dissertation (MD in Geology, International Institute for Geo-information Science and Earth Observation), 92.

[6]. Öztan, S. & Süzen, L. (2011). Mapping evaporite minerals by Aster. International Journal of Remote Sensing, 32, 1651-1673.

[7]. Orti-Cabo, F. (1976). An approach to the petrographical study of secondary gypsum microstructures and their origin. Dissertation (Diploma in sedimentary petrology, DJC, Imperial College, London), 140.

[8]. Attia, O. (1993). Sedimentological and petrological studies of the middle Miocene evaporites on the eastern side of the Gulf of Suez, Sinai, Egypt. Dissertation (PhD in geology, Cairo University, Cairo), 159.

[9]. Hosny, W., Gaafar, I. & Sabour, A. (1988). Miocene stratigraphic nomenclature in the Gulf of Suez region. Proceedings of the eighth Exploration Seminar, Cairo (1986), Egyptian General Petroleum Corporation, 1, 131-148.

[10]. Thiriet, J., Burollet, P., Montenat, C., & Ott D'estevou, P. (1986). Evolution tectonique et sedimentaire neogene a la transition du Golfe de Suez et de la Mer Rouge: La Secteur De Port-Safaga (Egypte). Documents Et Travaux, Institution Geology Albert De Lapparent, 10, 93–116.

[11]. Hume, W. (1921). Relations of the northern Red Sea and associated gulf areas to the "rift" theory. Proceedings of the Geology Society London, 77, 96-101.

[12]. Montenat, C., Ott D'estevou, P., Jarrige, J., & Richert, J. (1998). Rift development in the Gulf of Suez and the north-western Red Sea: Structural Aspects And Related Sedimentary Processes, Sedimentation And Tectonics In Rift Basins Red Sea: Gulf Of Aden. Springer Science and Business Media, ch. (B5), 97-116.

[13]. Jarrige, J., Ott D'estevou, P., & Sehans, P. (1986). Etude structural sur la marge occidentale de la Mer Rouge: le secteur du Gebel Duwi pres de Quseir (Egypte). Documents Et Travaux, Institution of Geology, Albert De L'apparent, 10, 117–127.

[14]. Van Dijk, J., Ajayi, A., De Vincenzi, L., Ellen, H., Guney, H., & Santoni, S. (2018). A new model for the development of the Gulf of Suez Rifting; Implications for hydrocarbon exploration and production potential, project: geology and geophysics of the exploration and production assets (Algeria, Tunesia, Egypt, Afghanistan, Iraq, Turkmenistan) of Dragon Oil (Enoc Group). Society of Petroleum Engineers, SPE- 192978-MS, 10.

[15]. Patton, T., Moustafa, A., Nelson, R., & Abdine, S. (1994). Tectonic evolution and structural setting of the Suez Rift (In Landon, S. Interior Rift Basins). AAPG Memoir, 59, 7–55.

[16]. Colletta, B., Le Quellec, P., Letouzey, J., & Moretti, I. (1988). Longitudinal evolution of the Suez Rift structure (Egypt). Tectonophysics, 153, 221–233.

[17]. Perry, S., & Schamel, S. (1990). The role of low-angle normal faulting and isostatic response in the evolution of the Suez Rift, Egypt. Tectonophysics, 174, 159–173.

[18]. Bosworth, W., & Mcclay, K. (2001). Structural and stratigraphic evolution of the Gulf of Suez Rift, Egypt: A synthesis (In Ziegler, P., Cavazza, W., Robertson, A. and Crasquin-Soleau, S. Peri-Tethys Memoir 6: Peri-Tethyan Rift/Wrench Basins and Passive Margins). Museum National D'histoire Naturelle De Paris, Memoir, 186, 567-606.

[19]. Moustafa, A. (1976). Block faulting in the Gulf of Suez. Proceedings of the fifth Egyptian General Petroleum Corporation Exploration Seminar, Cairo, 35.

[20]. Meshref, W., Refai, E., & Abdel Baki, S. (1976). Structural interpretation of the Gulf of Suez and its oil potentialities. Proceedings of the fifth Egyptian General Petroleum Corporation Exploration Seminar, Cairo, 21.

[21]. Moustafa, A. (1996). Internal structure and deformation of an accommodation zone in the northern part of the Suez Rift. Structural Geology, 18, 93-107.

[22]. Moustafa, A. (1998). Gebel Surf el Dara accommodation zone, southwestern part of the Suez Rift. Middle Eastern Research Center, Ain Shams University, Earth Science, 2, 227-239.

[23]. Amgad, I., & Mcclay, K. (2002). Development of accommodation zones in the Gulf of Suez-Red Sea Rift, Egypt. AAPG Bulletin, 86(6), 1003-1026.

[24]. Bosworth, W. (1985). Geometry of Propagating Continental Rifts. Nature, 316, 625-627.

[25]. Moustafa A. (2004). Explanatory notes for the geologic maps of the eastern side of the Suez Rift (Western Sinai Peninsula), Egypt. Ain Shams University, 34.

[26]. Peijs, J., Bevan, T., & Piombino, J. (2012). The Suez rift basin. In: Roberts, D., & Bally, A. (eds) Regional geology and tectonics: phanerozoic rift systems and sedimentary basins. 1st edition, Elsevier Publication, ch.(B), 165–194.

[27]. Evans, A. (1990). Miocene sandstone provenance relations in the Gulf of Suez: insights into synrift unroofing and uplift history. AAPG Bulletin, 74, 1386–1400.

[28]. Hantar, G. (1965). Remarks on the distribution of the Miocene sediments in the Gulf of Suez region. Proceedings of the fifth Arab Petroleum Congress, Cairo, Egypt, 13.

[29]. Saoudi, A., & Khalil, B. (1986). Distribution and hydrocarbon potential of Nukhul sediments in the Gulf of Suez. Proceedings of the seventh EGPC Exploration Seminar, 1984, 75–96.

[30]. Moustafa, A., & Khalil, S. (2017). Control of extensional transfer zones on syntectonic and posttectonic sedimentation: implications for hydrocarbon exploration. Journal of Geologic Society, London, 174, 318–335.

[31]. Garfunkel, Z., & Bartov, Y. (1977). The tectonics of the Suez rift. Geologic Survey Bulletin, 71, 44.

[32]. National Stratigraphic Sub-Committee of Egypt (1974). Rock-stratigraphy of the Miocene in the Gulf of Suez Region. Egyptian Journal of Geology, 1(1), 21-43.

[33]. Always, R., Tudoran, A., Knabe, K., Liu, C. & Strohmenger, C. (2002). New biostratigraphic and sequence stratigraphic constraints on Miocene synrift sequences from the northern Red Sea. Proceedings of the fifth Middle East Geoscience Conference, GEO 2002, GeoArab Abstract, 7(2), 208.

[34]. Bosworth, W., & McClay, K. (2001). Structural and stratigraphic evolution of the Suez rift, Egypt: a synthesis. In: Zeigler, P., Cavazza, W., Robertson, A., & Crasquin-Soleau, S. (eds) Peri-Tethyan rift-wrench basins and passive margins. Museum of National Histoire Naturelle, 567–606.

[35]. Evans, A. (1988). Neogene tectonic and stratigraphic events in the Suez rift area, Egypt. Tectonophysics, 153, 235–247.

[36]. Moon, F., & Sadek, H. (1923). Preliminary geological report on Wadi Gharandal area north of Gebel Hammam Faraun Western Sinai. Petroleum Research Bulletin, Cairo, 12, 42.

[37]. Awney, F., Hussein, R., & Nakhla, A. (1990). Blayim Marine and Land oil fields structural styles. Proceedings of the tenth EGPC Petroleim Exploration and Production Conference, 1, 400 –430.

[38]. Slater, P., Thome, K., Aria, K., Fujisada, H., Kieffer, H., Ono, A., Sakuma, F., Palluconi, F., & Yamaguchi, Y. (1995). Radiometric calibration of ASTER data. Journal of Japan Society for Remote Sensing, 15(2), 16-23.

[39]. Herman, B., & Browning, S. (1965). A numerical solution to the equation of radiative transfer. Journal Atmospheric Science, 22, 559-566.

[40]. Fujisada, H., Sakuma, F., Ono, A., & Kudoh, M. (1998). Design and pre-flight performance of aster instrument protoflight model. Transactions On Geoscience And Remote Sensing, 36(4), 1152 –1160.

[41]. Chrysoulakis, N., Abrams, M., Feidas, H., & Arai, K. (2010). Comparison of atmospheric correction methods using Aster data for the area of Crete, Greece. International Journal of Remote Sensing, 31(24), 6347–6385.

[42]. Du, Q., Gungor, O., & Shan, J. (2005). Evaluation for pan-sharpening techniques. Performance, 7803-9050, 3.

[43]. Ninomiya, Y. (2002). Mapping quartz, carbonate minerals, and mafic ultramafic rocks using remotely sensed multispectral thermal infrared ASTER data. Proceedings of SPIE, 191–203.

[44]. Shuai, S., Zhang, Z., Xinbiao, L., & Hao L. (2022). Assessment of new spectral indices and multi- seasonal ASTER data for gypsum mapping. Carbonates and Evaporites, 37(34), 19.

[45]. Pour, A., & Hashim, M. (2011). Application of advanced spaceborne thermal emission and reflection radiometer (ASTER) data in geological mapping. International Journal of Physics Science, 6, 7657 –7668.

[46]. Parashar, C. (2015). Mapping of alteration mineral zones by combining techniques of remote sensing and spectroscopy in the parts of se-rajasthan, Environmental Science, Geology. Indian institue of remote sensing, ISRO, department of space, Government of India

Dehradun. Dissertation (MD of technology in remote sensing and GIS, University of Andhra, India), 62.

[47]. Buhe, A., Tsuchiya, B., Kaneko, C., Ohtaishi, C., & Mahmut, H. (2007). Land cover of oases and forest in XinJiang, China retrieved from ASTER data Aosier. Advances in Space Research, 39, 39 – 45.

[48]. Salati, S., Van Ruitenbeek, F., Van der Meer, F., & Naimi, B. (2014). Detection of Alteration Induced by Onshore Gas Seeps from ASTER and WorldView-2 Data. Remote sensing, 6(4), 3188-3209.

[49]. Fakhari, S., Alireza, J., Peyman, A., & Mohammad, L. (2019). Delineation of hydrothermal alteration zones for porphyry systems utilizing ASTER data in Jebal-Barez area, SE Iran. Iran. Journal of Earth Sciences, 11, 80-92.

[50]. Bakardjiev, D., & Popov, K. (2015). ASTER spectral band ratios for detection of hydrothermal alterations and ore deposits in the Panagyurishte Ore Region, Central Srednogorie, Bulgaria. Advances in Space Research, pt.1, 76, 79–88.

[51]. Youssef, A., Hassan, A., & El-Haddad, A. (2009). Mapping of Prerift – Synrift Sedimentary units using Enhanced Thematic Mapper Plus (ETM+): Sidri – Feiran Area, Southwestern Sinai Peninsula, Egypt. Journal of Indian Society of Remote sensing, 37, 377–393.

[52]. Sabins, F. (1999). Remote Sensing for Mineral Exploration. Ore Geology Review, 14, 77-82.

[53]. Wahi, M., Taj-Eddine, K., & Laftouhi, N. (2013). ASTER VNIR and SWIR Band Enhancement for Lithological Mapping - A case study of the Azegour Area (Western High Atlas, Morocco). Journal of Environment and Earth Science, 3(12), 11.

[54]. Moradi, M., Basiri, S., Ali, K., & Kabiri, K. (2013). Fuzzy logic modeling for hydrothermal gold mineralization mapping using geochemical, geological, ASTER imageries and other geo-data, a case study in Central Alborz, Iran. Earth Science Information, 9.

[55]. Doğru, M., & Yücel, M. (2017). Araştırma Makalesi / Research Article LANDSAT 8 OLI Multispektral Verileri Kullanılarak Litolojik Harita Yapımı, Afyon Kocatepe Üniversitesi Fen ve Mühendislik Bilimleri Dergisi. AKU Journal of Science and Engineering, 17, 172-184.

[56]. Soha, J., & Schwartz, A. (1979). Multispectral Histogram Normalization Contrast Enhancement. Proceedings of Fifth Canadian Symposium of Remote Sensing, 86-93.

[57]. Gillespie, A., Kahle, A., & Walker, R. (1986). Color enhancement of highly correlated images-Decorrelation and HSI contrast stretches. Remote sensing and Environment, 20, 209–235.

[58]. Özyavaş, A. (2016). Assessment of image processing techniques and ASTER SWIR data for the delineation of evaporates and carbonate outcrops along the Salt Lake Fault, Turkey. International Journal of Remote sensing, 1366-5901.

[59]. Khan, A., Faisal, S., Shafique, M., Khan, S., & Sherbacha, A. (2020). Aster-based remote sensing investigation of gypsum in the Kohat Plateau, North Pakistan. Carbonates and Evaporites, 35(3), 13.

[60]. Kruse, F., Lefkoff, A., Boardman, J. (1993). The spectral image processing system (SIPS) interactive visualization and analysis of imaging spectrometer data. Remote sensing Environment, 44, 145 –163.

[61]. De Carvalho, O., & Meneses, P. (2000). Spectral correlation mapper (SCM): an improvement on the spectral angle mapper (SAM). Ninth JPL airborne earth science workshop, National Aeronautics and Space Administration of US, 9.

[62]. Ranganathan, P. & Siddan, A. (2020). Geospatial assessment of ultramafic rocks and ore minerals of Salem, India. Arabian Journal of Geosciences, 13, 1095.

نقشه برداری زمین شناسی و شناسایی رخساره تبخیرهای میوسن در امتداد حاشیه مرکزی شرقی خلیج سوئز ریفت با تکنیک های سنجش از دور

ایمان کامل*، محمد حمد و اسامه آتیا

دانشکده علوم، دانشگاه قاهره، قاهره، مصر

ارسال ۲۰۲۳/۰۹/۰۳، پذیرش ۲۰۲۳/۱۱/۱۰

* نویسنده مسئول مکاتبات: emanmostafa454@gmail.com

چکیده:

در سال‌های اخیر، استفاده از داده‌های ASTER و Landsat برای نقشه برداری انواع مختلف سازندهای سنگی رایج شده است. به طور خاص، این مطالعه از تصاویر ASTER (L1B) و Landsat 8 (AOL) برای نقشه‌برداری رخنمون‌های رخساره‌های مختلف گچی در منطقه راس ملاب در غرب مرکزی سینا استفاده می‌کند. این رخساره‌های گچی بخشی از یک گروه سنگ چینه شناسی به نام Ras Malaab هستند که تخمین زده می‌شود در دوره میوسن تشکیل شده باشند. طیف وسیعی از تکنیک‌های پردازش تصویر برای ایجاد نقشه رخساره‌های نهایی از جمله شاخص‌های کوارتز و سولفات، ترکیب باندهای تصویر مرکب، نسبت‌های باند، تجزیه و تحلیل اجزای اصلی، کشش همبستگی، و نقشه‌برداری SAM به‌دنبال طبقه‌بندی نظارت شده استفاده شد. با استفاده از ترکیبات نواری، شاخص‌های معدنی و آنالیز اجزای اصلی، کانی‌های سولفاتی از محیط اطرافشان متمایز شدند. علاوه بر این، کشش‌های همبستگی و نسبت‌های نواری برای تمایز بین گچ اولیه، ثانویه، گسل‌دار، انیدریت و کربنات‌ها استفاده شد. الگوریتم نقشه برداری سریع SAM نیز ابزار مؤثری برای تمایز بین رخساره‌های اصلی در منطقه مورد مطالعه و تمایز بین گچ توده‌ای اولیه و گچ بستر بود. نتایج این مطالعه با ایجاد نقشه رخساره‌ای منطقه با استفاده از طبقه‌بندی نظارت شده خلاصه شد که علاوه بر مطالعات سنگ‌نگاری، به درک پراکندگی رخساره‌های مختلف گچی کمک زیادی کرد.

کلمات کلیدی: شاخص سولفات، گچ، نقشه برداری رخساره.